Magnetic Resonance Imaging 57 (2019) 235–242

Contents lists available at ScienceDirect

Magnetic Resonance Imaging

journal homepage: www.elsevier.com/locate/mri

Original contribution

Diffusion MRI detects longitudinal white matter changes in the 3xTg-AD mouse model of Alzheimer's disease

Xingju Nie[a,b,*,1], Maria Fatima Falangola[a,b,1], Ralph Ward[c], Emilie T. McKinnon[a,b,d], Joseph A. Helpern[a,b,d,e], Paul J. Nietert[c], Jens H. Jensen[a,b,e]

[a] Department of Neuroscience, Medical University of South Carolina, Charleston, SC, USA
[b] Center for Biomedical Imaging, Medical University of South Carolina, Charleston, SC, USA
[c] Department of Public Health Sciences, Medical University of South Carolina, Charleston, SC, USA
[d] Department of Neurology, Medical University of South Carolina, Charleston, SC, USA
[e] Department of Radiology and Radiological Science, Medical University of South Carolina, Charleston, SC, USA

ARTICLE INFO

Keywords:
Diffusion MRI
Diffusional kurtosis imaging
3xTg-AD mouse
White matter
Alzheimer's disease

ABSTRACT

The sensitivity of multiple diffusion MRI (dMRI) parameters to longitudinal changes in white matter microstructure was investigated for the 3xTg-AD transgenic mouse model of Alzheimer's disease, which manifests both amyloid beta plaques and neurofibrillary tangles. By employing a specific dMRI method known as diffusional kurtosis imaging, eight different diffusion parameters were quantified to characterize distinct aspects of water diffusion. Four female 3xTg-AD mice were imaged at five time points, ranging from 4.5 to 18 months of age, and the diffusion parameters were investigated in four white matter regions (fimbria, external capsule, internal capsule and corpus callosum). Significant changes were observed in several diffusion parameters, particularly in the fimbria and in the external capsule, with a statistically significant decrease in diffusivity and a statistically significant increase in kurtosis. Our preliminary results demonstrate that dMRI can detect microstructural changes in white matter for the 3xTg-AD mouse model due to aging and/or progression of pathology, depending strongly on the diffusion parameter and anatomical region.

1. Introduction

Diffusion MRI (dMRI) is widely used as a noninvasive means of detecting changes in brain tissue microstructure associated with both pathology and aging [1]. Its sensitivity to microstructure stems from its ability to quantify the motion of water molecules on length scales commensurate with the size of neurons and glia.

For Alzheimer's disease (AD), dMRI holds promise as a method of monitoring disease progression that is potentially useful in assessing the efficacy of drug therapies. To better understand the meaning of alterations of diffusion parameters in the context of AD, dMRI experiments with transgenic mouse models of AD pathology are valuable in allowing for controlled studies from the earliest stages of disease.

Several different transgenic mouse models have contributed substantially to our understanding of AD pathogenesis [2,3]. Among them is the triple transgenic AD mouse model (3xTg-AD) that progressively develops amyloid and tau-related pathologies with a temporal and regional-specific profile comparable to human AD pathology [4,5]. This model has been applied extensively to investigate AD [6–11], including for a few prior imaging studies [12–15]. 3xTg-AD mice show intracellular accumulation of amyloid beta (Aβ) at 3 months of age, with extracellular plaques appearing in the neocortex and hippocampus at 6 months of age. Tau pathology begins at 6 months, when phosphorylated tau becomes detectable in the hippocampus, and develops into neurofibrillary tangles after 12 months of age [4,5,16]. Interestingly, the first detectable pathological features in this model are alterations in overall myelination patterns leading to white matter (WM) disruption. Changes in oligodendrocyte and myelin marker

Abbreviations: AD, Alzheimer's disease; Aβ, amyloid beta; WM, white matter; DK, diffusional kurtosis; DKI, diffusional kurtosis imaging; DT, diffusion tensor; DTI, diffusion tensor imaging; FA, fractional anisotropy; MD, mean; ($D_{\|}$), axial diffusivities; ($D_{\perp}$), radial diffusivities; KFA, kurtosis fractional anisotropy; MK, mean; ($K_{\|}$), axial kurtoses; ($K_{\perp}$), radial kurtoses; Fi, fimbria; EC, external capsule; IC, internal capsule; CC, corpus callosum; GLMMs, general linear mixed models

* Corresponding author at: Department of Neuroscience, Center for Biomedical Imaging, Medical University of South Carolina, 173 Ashley Avenue, BSB 403, MSC 510, Charleston, SC 29425, USA.
E-mail address: niexi@musc.edu (X. Nie).

[1] These authors contributed equally to the work.

https://doi.org/10.1016/j.mri.2018.12.003
Received 18 September 2018; Received in revised form 19 November 2018; Accepted 8 December 2018

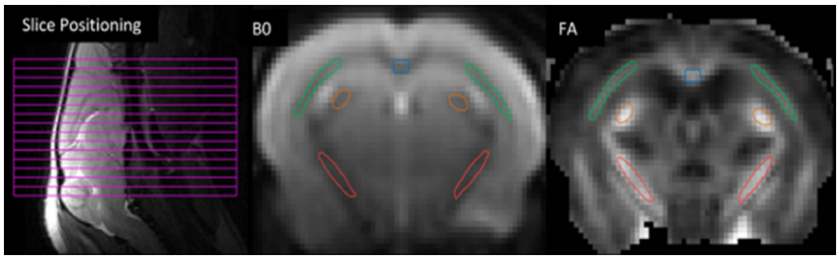

Fig. 1. The position of the 15 coronal slices for the dMRI acquisition is shown in the leftmost image. Examples of the four white matter ROIs used in the data analysis are shown on the average b-value = 0 image (middle image) and on the FA map (right image). The corpus callosum (CC — blue), fimbria (Fi — orange), external (EC — green) and internal (IC — red) capsule were manually drawn on the b-value = 0 image and verified with the FA maps to ensure correct anatomical location. (For interpretation of the references to color in this figure legend, the reader is referred to the web version of this article.)

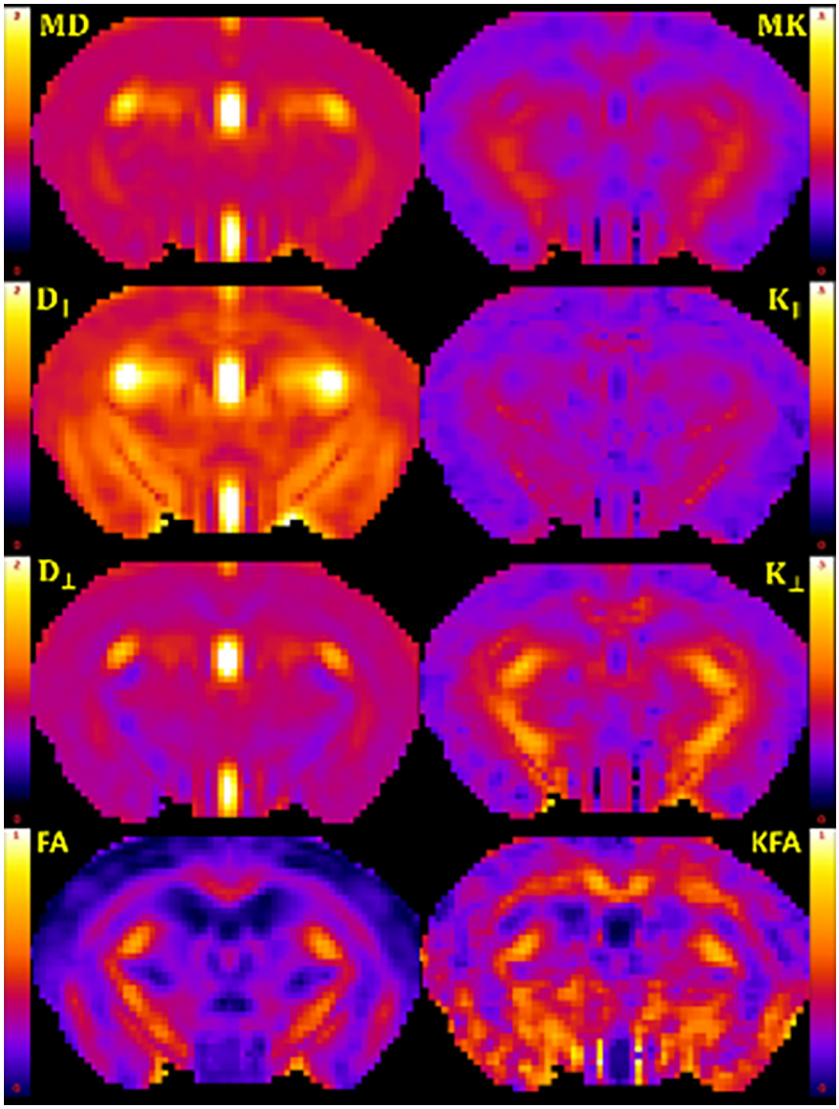

Fig. 2. Representative dMRI parametric maps of all considered diffusion measures for a single anatomical slice from one mouse brain. The left column shows the DT measures of mean diffusivity (MD), axial diffusivity ($D_{\parallel}$), radial diffusivity ($D_{\perp}$) and fractional anisotropy (FA), while the right column shows the DK measures of mean kurtosis (MK), axial kurtosis ($K_{\parallel}$), radial kurtosis ($K_{\perp}$) and kurtosis fractional anisotropy (KFA). Scale bars: 0–1 for FA and KFA; 0–2 μm^2/ms for MD, $D_{\parallel}$ and $D_{\perp}$; 0–3 for MK, $K_{\parallel}$, and $K_{\perp}$.

expression are noticeable in the hippocampus and entorhinal cortex as early as 2 months of age [17–19] and precede the first cognitive impairments and Aβ plaques [17].

Despite these well characterized morphological and histochemical WM matter abnormalities, only one prior dMRI study has investigated WM in the 3xTg-AD mouse model [14]. Employing the specific dMRI method of diffusion tensor imaging (DTI), this study reported no WM differences in older (11–17 months) 3xTg-AD mice relative to controls.

Diffusional kurtosis imaging (DKI) is an alternative dMRI technique that extends DTI by quantifying the non-Gaussian behavior of water diffusion, contributing additional information beyond what is given by DTI [20,21]. Besides the diffusion indices conventionally obtained with DTI, DKI also provides measures of diffusional non-Gaussianity, such as mean (MK), axial ($K_{\parallel}$) and radial ($K_{\perp}$) kurtoses. These extra parameters can help to characterize both normal and abnormal brain tissue cytoarchitecture. DKI has been used in human studies to investigate tissue microstructural changes associated with aging [22–25] and AD [26,27], particularly for assessing WM abnormalities [28–31]. Furthermore, the

Table 1
Mean value ± standard deviation for all imaging time-points observed for each diffusion measure by ROI. Mean (MD), axial ($D_{\parallel}$) and radial ($D_{\perp}$) diffusivities, fractional anisotropy (FA), mean (MK), axial ($K_{\parallel}$), and radial ($K_{\perp}$) kurtoses and kurtosis fractional anisotropy (KFA).

Region of interest	Diffusion measures (mean ± SD)							
	MD (μm^2/ms)	$D_{\parallel}$ (μm^2/ms)	$D_{\perp}$ (μm^2/ms)	FA	MK	$K_{\parallel}$	$K_{\perp}$	KFA
Fimbria (Fi)								
4.5 months	0.96 ± 0.03	1.68 ± 0.07	0.60 ± 0.03	0.58 ± 0.02	1.16 ± 0.03	0.85 ± 0.00	1.86 ± 0.05	0.58 ± 0.02
9 months	0.94 ± 0.02	1.68 ± 0.03	0.57 ± 0.02	0.60 ± 0.01	1.18 ± 0.04	0.84 ± 0.03	1.96 ± 0.08	0.60 ± 0.03
12 months	0.91 ± 0.02	1.64 ± 0.06	0.55 ± 0.01	0.60 ± 0.02	1.22 ± 0.05	0.89 ± 0.02	2.04 ± 0.12	0.62 ± 0.01
15 months	0.89 ± 0.05	1.60 ± 0.07	0.53 ± 0.04	0.61 ± 0.01	1.24 ± 0.05	0.91 ± 0.04	2.11 ± 0.06	0.63 ± 0.04
18 months	0.88 ± 0.02	1.57 ± 0.03	0.53 ± 0.02	0.60 ± 0.01	1.26 ± 0.04	0.94 ± 0.03	2.05 ± 0.07	0.62 ± 0.02
External capsule (EC)								
4.5 months	0.79 ± 0.03	1.03 ± 0.03	0.68 ± 0.02	0.30 ± 0.01	0.89 ± 0.04	0.81 ± 0.03	0.98 ± 0.06	0.42 ± 0.03
9 months	0.78 ± 0.04	1.00 ± 0.06	0.66 ± 0.03	0.30 ± 0.01	0.90 ± 0.03	0.80 ± 0.02	1.01 ± 0.05	0.42 ± 0.03
12 months	0.78 ± 0.04	1.01 ± 0.05	0.66 ± 0.04	0.30 ± 0.01	0.92 ± 0.05	0.81 ± 0.01	1.05 ± 0.07	0.42 ± 0.05
15 months	0.76 ± 0.03	0.99 ± 0.04	0.64 ± 0.02	0.31 ± 0.01	0.93 ± 0.02	0.83 ± 0.02	1.03 ± 0.04	0.44 ± 0.03
18 months	0.75 ± 0.01	0.98 ± 0.02	0.64 ± 0.01	0.30 ± 0.01	0.96 ± 0.03	0.88 ± 0.04	1.07 ± 0.04	0.42 ± 0.01
Internal capsule (IC)								
4.5 months	0.77 ± 0.02	1.26 ± 0.03	0.53 ± 0.02	0.50 ± 0.02	1.22 ± 0.01	0.96 ± 0.03	1.69 ± 0.04	0.53 ± 0.03
9 months	0.77 ± 0.01	1.27 ± 0.02	0.52 ± 0.01	0.51 ± 0.01	1.23 ± 0.03	0.93 ± 0.02	1.73 ± 0.06	0.53 ± 0.03
12 months	0.77 ± 0.01	1.26 ± 0.02	0.52 ± 0.01	0.51 ± 0.01	1.21 ± 0.01	0.93 ± 0.02	1.74 ± 0.01	0.54 ± 0.02
15 months	0.74 ± 0.01	1.22 ± 0.02	0.51 ± 0.01	0.51 ± 0.02	1.21 ± 0.06	0.94 ± 0.05	1.72 ± 0.11	0.55 ± 0.02
18 months	0.75 ± 0.01	1.22 ± 0.05	0.52 ± 0.02	0.50 ± 0.03	1.26 ± 0.09	1.00 ± 0.06	1.74 ± 0.11	0.53 ± 0.05
Corpus callosum (CC)								
4.5 months	0.77 ± 0.03	1.01 ± 0.03	0.65 ± 0.03	0.40 ± 0.02	1.00 ± 0.05	0.94 ± 0.06	1.23 ± 0.11	0.54 ± 0.04
9 months	0.78 ± 0.02	1.05 ± 0.03	0.64 ± 0.02	0.42 ± 0.02	1.04 ± 0.03	1.01 ± 0.03	1.26 ± 0.07	0.54 ± 0.04
12 months	0.78 ± 0.03	1.03 ± 0.04	0.65 ± 0.02	0.41 ± 0.02	1.05 ± 0.03	1.00 ± 0.05	1.23 ± 0.09	0.52 ± 0.01
15 months	0.74 ± 0.01	0.99 ± 0.01	0.62 ± 0.01	0.42 ± 0.01	1.02 ± 0.04	1.01 ± 0.03	1.19 ± 0.02	0.55 ± 0.03
18 months	0.75 ± 0.02	0.99 ± 0.01	0.64 ± 0.03	0.42 ± 0.02	1.04 ± 0.06	1.05 ± 0.06	1.15 ± 0.08	0.53 ± 0.05

Fig. 3. Summary of qualitative trends: vertical arrows represent a metric in which all mice exhibited the same trend between time-points one (4.5 months) and five (18 months); diagonal arrows indicate that one mouse had a contrary trend, while horizontal arrows indicate no clear trend. Mean (MD), axial ($D_{\parallel}$) and radial ($D_{\perp}$) diffusivities, fractional anisotropy (FA), mean (MK), axial ($K_{\parallel}$), and radial ($K_{\perp}$) kurtoses and kurtosis fractional anisotropy (KFA). Fimbria (Fi), external capsule (EC), internal capsule (IC) and corpus callosum (CC).

extra diffusional kurtosis (DK) measures have a demonstrated sensitivity to brain pathology in a variety of animal models [32–34], including AD mouse models [35,36].

Thus, the goal of this study was to investigate the sensitivity of DKI to WM microstructural changes associated with age and different stages of disease progression in the 3xTg-AD mouse model.

2. Methods

2.1. AD mouse model

All experimental procedures were approved by the Institutional Animal Care and Use Committee at Medical University of South Carolina (MUSC) and conducted in accordance with the National Institutes of Health (NIH) Guide for Care and Use of Laboratory Animals. Four female 3xTg-AD mice were studied longitudinally at 4.5, 9, 12, 15 and 18 months of age. The 3xTg-AD mice possess three mutations of human presenilin-1 M146 V, human amyloid precursor protein Swedish mutation, the P301L mutation of human tau, and develop both Aβ and neurofibrillary tangles (NFTs) in a temporal and spatial pattern that is similar to human AD pathology. All mice were housed in temperature- and humidity-controlled rooms on a 12-h light/dark cycle (lights on at 6:00 AM) in an accredited animal care facility.

2.2. MRI acquisition

Mice were anesthetized using an isoflurane vaporizer set at the following percentages: 3% for induction, 2% during pilot scanning, and 1.5% during data acquisition. An animal monitoring unit (SA Instruments, Inc., model 1025, Stony Brook, NY) was used to record respiration and rectal temperature. Respiration was measured with a pressure transducer placed under the abdomen just below the ribcage. Body temperature was maintained using ventilated warm air, controlled by a feedback circuit between the heater and thermistor. After induction, mice were placed on a mouse holder and restrained using a mouse tooth bar (Bruker, T10146) and ear bars (Bruker, T10147) placed in the auditory canal. Compressed air was used as the carrier gas and delivered at a flow rate (1 L/min) to a nose cone positioned around the tooth bar, where gases mixed with air and passed over the rodent's nose. All animals were maintained at 37.0 ± 0.2 °C and respiration

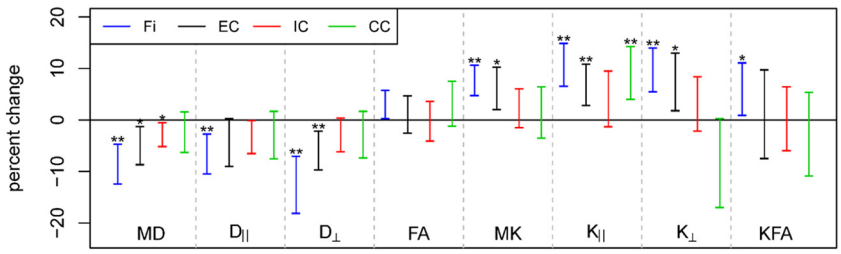

Fig. 4. Estimated percent changes for all diffusion measures over the time interval between 4.5 months and 18 months for each ROI, shown as 95% confidence intervals. All changes were calculated using GLMMs and the full dataset of 5 time points. Significant differences are indicated by * ($p < 0.05$) and ** ($p < 0.01$). Mean (MD), axial ($D_{\|}$) and radial ($D_{\perp}$) diffusivities, fractional anisotropy (FA), mean (MK), axial ($K_{\|}$), and radial ($K_{\perp}$) kurtoses and kurtosis fractional anisotropy (KFA). Fimbria (Fi), external capsule (EC), internal capsule (IC) and corpus callosum (CC).

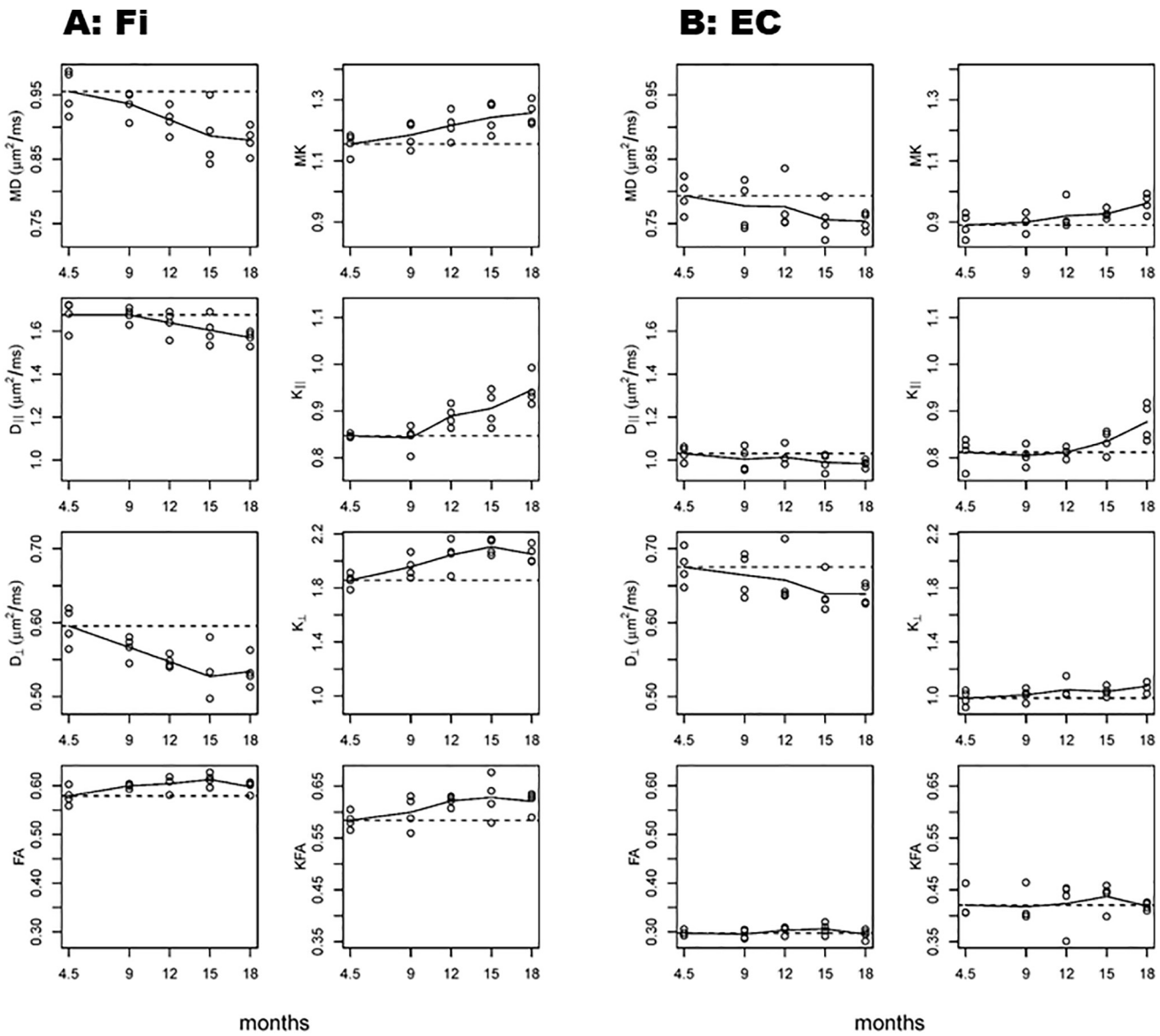

Fig. 5. Individual data points and average temporal trajectories for all diffusion measures in each ROI. Pronounced changes are seen in the fimbria (A) and to a somewhat lesser extent in the external capsule (B) for most of the parameters. In contrast, the internal capsule (C) and corpus callosum (D) both showed relatively less variation with time. Mean (MD), axial ($D_{\|}$) and radial ($D_{\perp}$) diffusivities, fractional anisotropy (FA), mean (MK), axial ($K_{\|}$), and radial ($K_{\perp}$) kurtoses and kurtosis fractional anisotropy (KFA).

ranged between 70 and 80 breaths per minute during scanning.

The *in vivo* MRI experiments were performed on a 7 T BioSpec 70/30 horizontal scanner (Bruker BioSpin, Ettlingen, Germany) running Paravision 5.1 acquisition software, and equipped with a 12 cm inner diameter actively shielded gradient system (440 mT/m) with a quadrature volume coil (T128038) for signal transmission and a mouse brain array coil (T11765) for signal reception. A 2-shot spin-echo echo planar imaging (SE-EPI) sequence was used for DKI acquisition. Sequence parameters were: TR/TE = 3750/32.6 ms, δ/Δ = 5/18 ms, slice thickness = 0.7 mm, 15 coronal slices with no gap (Fig. 1), data matrix = 128 × 128, image resolution = 156 × 156 μm^2, 2 repetitions, 10 b-value = 0 images, followed by 30 diffusion encoding gradient directions with 4 b-values for each gradient direction (0.5, 1, 1.5, 2 ms/μm^2), and fat suppression using a frequency selective RF pulse with a flip angle of 105° to minimize chemical shift artifacts. Total acquisition time = 33 min.

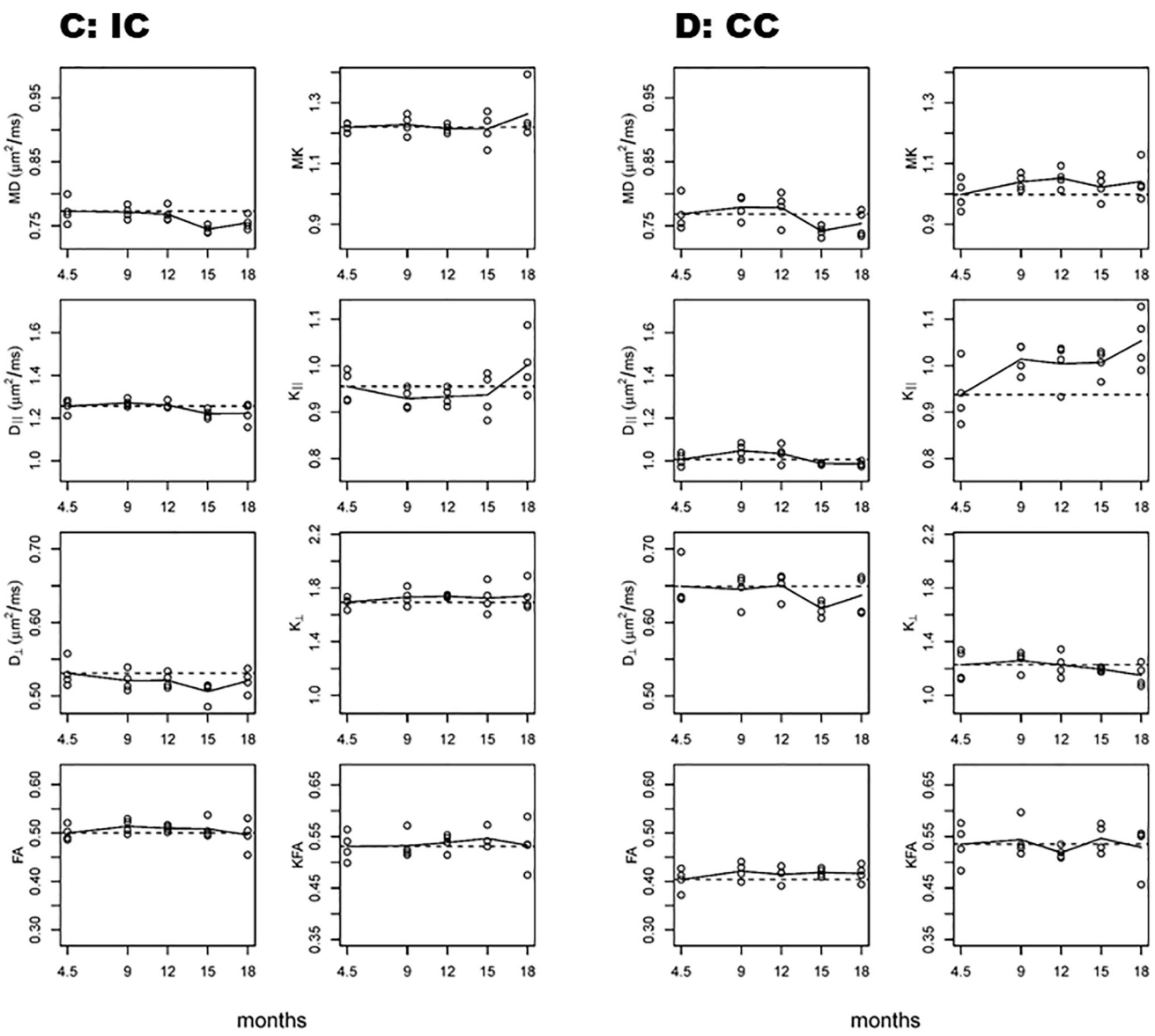

Fig. 5. (*continued*)

2.3. DKI post-processing and image analysis

DKI post-processing was performed using DKE [37] (http://nitrc.org/projects/dke). Parametric maps were obtained by fitting dMRI signal measurements to the DKI signal model for each voxel using a linearly constrained weighted linear least squares fitting algorithm, which generated the diffusion and kurtosis tensors. These two tensors were then used to calculate parametric maps for all diffusion measures [20,38]. In our analysis, we considered the four diffusion tensor (DT) parameters of mean diffusivity (MD), axial diffusivity ($D_{\parallel}$), radial diffusivity ($D_{\perp}$), and fractional anisotropy (FA). MD corresponds to the diffusivity averaged over all diffusion directions, $D_{\parallel}$ corresponds to the diffusivity in the direction of the principal diffusion tensor eigenvector, $D_{\perp}$ corresponds to the diffusivity averaged over all diffusion directions perpendicular to the principal diffusion tensor eigenvector, and FA quantifies the anisotropy of the diffusion tensor. We similarly considered the four DK parameters of mean kurtosis (MK), axial kurtosis ($K_{\parallel}$), radial kurtosis ($K_{\perp}$), and kurtosis fractional anisotropy (KFA). These are kurtosis analogs of the DT metrics that quantify diffusional non-Gaussianity and provide complementary information about the diffusion dynamics [20,38,39]. All 4 b-values for each gradient direction (0.5, 1, 1.5, 2 ms/μm^2) were used for calculating all the diffusion parameters. It is worth noting that, due to the inclusion of non-Gaussian effects, the DKI yields more accurate estimates of DT metrics than DTI itself [40], as well as enabling a more comprehensive assessment of the diffusion microenvironment in brain tissue.

Regions of interest (ROIs) were defined for the corpus callosum (CC), fimbria (Fi), external (EC) and internal (IC) capsule, which are WM tracks relevant to age-related changes and in AD pathology. These were manually drawn on the averaged b-value = 0 image by a neuropathologist (MFF), using ImageJ (http://rsb.info.nih.gov/) [41]. Anatomical guidelines for outlining these regions were determined by comparing anatomical structures in the MRI slices with a standard mouse atlas [42] and verified with the FA maps to ensure correct anatomical location and to avoid contamination of unintended tissue or cerebrospinal fluid (CSF). Slice positioning and sample ROIs for one animal are shown in Fig. 1. The mean regional value for each diffusion metric was obtained by averaging over all the voxels within a given ROI using ImageJ.

2.4. Statistical analyses

General linear mixed models (GLMM) were used to model each diffusion metric separately, with age and ROI as predictors. The

covariance structure within each mouse was estimated using the direct product of distinct covariance structures for ROI and age. ROI had an unstructured covariance which was inferred from the data, while age had an autoregressive covariance, meaning that the correlation between measurements at the earliest age and those at each successive age became less with time. Since the region-specific metrics represent means of many voxel-specific measures, the observations were weighted based on the inverse of the region-specific standard deviation for each mouse over each diffusion metric; this process generally provided superior model fit based on the Akaike Information Criterion [43] when compared to unweighted or inverse-variance weighted analyses. SAS v9.4 (SAS Institute, Cary, NC) was used to construct the linear mixed models, and R (version3.4.3) was used for graphical purposes. All reported p values were considered statistically significant at $p < 0.05$.

3. Results

Representative parametric maps of all considered diffusion measures for a single anatomical slice from one mouse brain are shown in Fig. 2. Note that the diffusivities have units of $\mu m^2/ms$, while the other parameters are dimensionless. Both the anisotropies and kurtoses are generally elevated in WM relative to gray matter, reflecting the distinct microstructural characteristics of these two types of brain tissue.

Table 1 shows, for all of the ROIs, the mean values ± standard deviations of each diffusion measure of each diffusion measure at each imaging time-point. The qualitative trends for the different quantities between time-points one and five are depicted in Fig. 3. For the ROIs studied, we observed that MD, $D_{\parallel}$ and $D_{\perp}$ generally decreased with age, while MK, $K_{\parallel}$ and $K_{\perp}$ generally increased. KFA and FA remained unchanged, except for the Fi region, which showed a trend for increase. Changes in all diffusion measures were more pronounced in the Fi and EC regions.

Fig. 4 summarizes results from the GLMMs, showing the estimated percent change for each diffusion metric between time-points one (4.5 months) and five (18 months) for each ROI. In the Fi, significant changes were observed for all but one diffusion parameter (MD, $D_{\perp}$, $D_{\parallel}$, MK, KFA, $K_{\parallel}$ and $K_{\perp}$), while five diffusion parameters (MD, $D_{\perp}$, MK, $K_{\parallel}$ and $K_{\perp}$) reached significance in the EC. In contrast, only one diffusion parameter showed significant changes in the IC (MD) and CC ($K_{\parallel}$). Both the MD and $K_{\parallel}$, had significant changes in three of the four regions, while the FA did not exhibit significant alterations in any of the ROI.

The individual data points together with the average temporal trajectories for all diffusion parameters in each ROI are illustrated in Fig. 5. The most pronounced differences are seen in the Fi region, with all measures other than the FA displaying clear changes. Our data suggest that differences relative to the initial time point are already apparent in the Fi when the mice are 9 months-old.

4. Discussion

Significant changes occur for several diffusion measures in WM of 3xTg-AD mice over the age range of 4.5 to 18 months, which demonstrates the ability of dMRI to detect alterations in WM microstructure for this transgenic model associated with aging and/or pathology. As a consequence, dMRI is a viable tool for assessing disease progression and the impact of potential therapies on WM morphology in 3xTg-AD mice, with the advantages of being non-invasive and able to sample the entire brain.

Several biological processes may underlie the longitudinal dMRI changes reported here. Morphological changes such as myelin breakdown, increase in axonal membrane permeability, decrease in the density of myelinated axons and fiber loss are all possible. Increased extracellular space, cell swelling and the presence of inflammatory cells may also have an impact upon water diffusion. However, only a dMRI study with a temporal morphological characterization of this model will be able to identify the specific pathological feature and elucidate the underlying mechanisms for each dMRI metric change and specific brain region.

The observed changes were much more pronounced in some anatomical regions than others. In particular, the Fi and EC were significantly altered in seven and five out of the eight diffusion measures considered, respectively, while only a single diffusion parameter was altered in the IC and in the CC. We also found large variability in the sensitivity of the various diffusion measures with MD and $K_{\parallel}$ being the most sensitive to change, highlighting the advantage of employing multiple parameters.

It should also be noted that all diffusivity measures with significant differences decreased with age, while all kurtosis measures with significant differences increased with age. Since our study did not include a control group it was not possible to determine the extent to which the observed dMRI changes are directly related to aging rather than to different stages of disease progression or both. However, since age-related changes usually lead to increases in water diffusivity [44–46], and our results showed a decrease in diffusivity metrics associated with an increase in kurtosis metrics, it is likely that a pathological component is associated with these changes. Additionally, since the dMRI changes seem to start when mice are around 9 months old (Fig. 5), when both intraneuronal Aβ and extracellular amyloid deposits are present both in the cortex and hippocampus, it suggests that, at least in part, the WM changes occur along with the progression of AD-like pathology. However, a dMRI study with a temporal morphological characterization of this model is needed to confirm this hypothesis.

Previous dMRI studies have reported similar trends of decrease in diffusivity and increase in kurtosis in the brain using different mouse models of AD [35,36,45,46]. Our diffusion tensor (DT) metrics results are in general concordance with Sun et al. [45], where reduced $D_{\perp}$ with age in the EC of the transgenic group (APPsw) is seen in the results. However, they also reported reduced $D_{\parallel}$ in the CC which contrasts with our finding of no CC change. Also, our results contrast with Sahara et al. [46], where an age-related FA decrease is reported in several WM fiber tracks, including CC and Fi, but our results did not show FA change in any of the regions examined. Additionally, the two DKI studies in a mouse model of AD [35,36] examined mostly gray matter regions showing an overall increase of MK and $K_{\parallel}$ in the cortex of APP/PS1 mice. The only WM region examined was the CC [36], and they reported an age-related decrease in FA at the genu of the CC and an age-related increase in FA at the body and splenium of the CC. However, it should be noted that important methodological factors distinguish our study from all these prior investigations, making it difficult to directly compare results.

The only other dMRI study assessing the 3xTg-AD mouse model did not find statistically significant changes in WM between transgenic mice and controls [14], but in contrast to our study, no age-related differences in trajectories are reported, only group comparisons. Several other methodological factors distinguish this prior work from ours. In our study, we used only female mice, while in Ref. [14] both male and female mice were used. Since pathology is more variable and far less pronounced in male 3xTg-AD mice [47,48], this may have reduced their ability to detect WM changes. Additionally, ROIs were sampled differently; in Ref. [14], the CC and EC were combined, and the Fi was not assessed. Finally, we used DKI, which provides a more comprehensive characterization of water diffusion than DTI. In fact, more significant differences were observed for the DK measures than for the DT measures, highlighting the additional sensitivity to microstructural changes that DKI provides.

The results presented here reveal, for the first time, age and/or pathology related WM changes in the brain of 3xTg-AD mice using DKI. In our study, the most pronounced changes occurred at the Fi region. Myelinated axons coming from neurons in the subiculum and hippocampus will form the alveus and aggregates to form the Fi, which will proceed upward to form the fornix [49,50]. The fimbria-fornix fibers

acts as the major output tract of the hippocampus and play an important role in the formation and consolidation of memories, and they have been shown to be vulnerable to aging as well as AD pathology [30,51–55]. Thus, the decrease in diffusivity metrics associated with an increase in kurtosis metrics in the Fi of the 3xTg-AD mice probably reflects the AD pathology progression in the hippocampus.

The main limitations of this preliminary study are the small number of mice studied and the absence of a normal control group. However, our principal goal was to investigate the sensitivity of dMRI for detecting alterations in WM microstructure at different pathological stages of the 3xTg-AD model, and we found significant diffusion changes over time in this model despite these limitations.

5. Conclusion

We have demonstrated that alterations in WM microstructure due to aging and/or the progression of pathology in 3xTg-AD mice can be detected with dMRI. Thus, dMRI is a viable tool for monitoring the effects of therapeutic interventions on brain tissue in this model. However, changes in diffusion measures were only observed in some anatomical regions, with the most pronounced differences being seen in the fimbria, and the several diffusion measures considered showed a variable sensitivity. The inclusion of kurtosis parameters, made possible by the use of DKI, resulted in more significant differences being observed, and it may therefore be advantageous to employ this extension of DTI in dMRI studies of the 3xTg-AD model.

Acknowledgements

The authors thank Dr. Salvatore Oddo of Arizona State University for the generous gift of the 3xTg-AD mice. This work was supported by the National Institutes of Health (1RF1AG057602-01) to M.F.F and J.H.J, T32DC014435 (to J. Dubno) and The Litwin Foundation to J.A.H.

Declarations of interest

None.

References

[1] Le Bihan D, Johansen-Berg H. Diffusion MRI at 25: exploring brain tissue structure and function. Neuroimage 2012 Jun 1;61(2):324–41.
[2] Theuring F, Thunecke M, Kosciessa U, Turner JD. Transgenic animals as models of neurodegenerative diseases in humans. 151. 1997. p. 320–5.
[3] Webster SJ, Bachstetter AD, Nelson PT, Schmitt FA, Van Eldik LJ. Using mice to model Alzheimer's dementia: an overview of the clinical disease and the preclinical behavioral changes in 10 mouse models. Front Genet 2014;5:88https://doi.org/10.3389/fgene.2014.00088.
[4] Oddo S, Caccamo A, Shepherd JD, Murphy MP, Golde TE, Kayed R, et al. Triple-transgenic model of Alzheimer's disease with plaques and tangles: intracellular Abeta and synaptic dysfunction. Neuron 2003;39:409–21.
[5] Oddo S, Caccamo A, Tran L, Lambert MP, Glabe CG, Klein WL, et al. Temporal profile of amyloid-beta (Abeta) oligomerization in an in vivo model of Alzheimer disease. A link between Abeta and tau pathology. J Biol Chem 2006;281:1599–604. https://doi.org/10.1074/jbc.M507892200.
[6] Halagappa VK, Guo Z, Pearson M, Matsuoka Y, Cutler RG, Laferla FM, et al. Intermittent fasting and caloric restriction ameliorate age-related behavioral deficits in the triple-transgenic mouse model of Alzheimer's disease. Neurobiol Dis 2007;26:212–20. https://doi.org/10.1016/j.nbd.2006.12.019.
[7] Mastrangelo MA, Bowers WJ. Detailed immunohistochemical characterization of temporal and spatial progression of Alzheimer's disease-related pathologies in male triple-transgenic mice. BMC Neurosci 2008;9:81. https://doi.org/10.1186/1471-2202-9-81.
[8] Ghosh D, Levault KR, Barnett AJ, Brewer GJ. A reversible early oxidized redox state that precedes macromolecular ROS damage in aging nontransgenic and 3xTg-AD mouse neurons. J Neurosci 2012;32:5821–32. https://doi.org/10.1523/JNEUROSCI.6192-11.2012.
[9] Dunn HC, Ager RR, Baglietto-Vargas D, Cheng D, Kitazawa M, Cribbs DH, et al. Restoration of lipoxin A4 signaling reduces Alzheimer's disease-like pathology in the 3xTg-AD mouse model. J Alzheimers Dis 2015;43:893–903. https://doi.org/10.3233/JAD-141335.
[10] Stover KR, Campbell MA, Van Winssen CM, Brown RE. Early detection of cognitive deficits in the 3xTg-AD mouse model of Alzheimer's disease. Behav Brain Res 2015;289:29–38. https://doi.org/10.1016/j.bbr.2015.04.012.
[11] Clark JK, Furgerson M, Crystal JD, Fechheimer M, Furukawa R, Wagner JJ. Alterations in synaptic plasticity coincide with deficits in spatial working memory in presymptomatic 3xTg-AD mice. Neurobiol Learn Mem 2015;125:152–62. https://doi.org/10.1016/j.nlm.2015.09.003.
[12] Takano T, Han X, Deane R, Zlokovic B, Nedergaard M. Two-photon imaging of astrocytic Ca^{2+} signaling and the microvasculature in experimental mice models of Alzheimer's disease. Ann N Y Acad Sci 2007;1097:40–50. https://doi.org/10.1196/annals.1379.004.
[13] Lin AJ, Koike MA, Green KN, Kim JG, Mazhar A, Rice TB, et al. Spatial frequency domain imaging of intrinsic optical property contrast in a mouse model of Alzheimer's disease. Ann Biomed Eng 2011;39:1349–57. https://doi.org/10.1007/s10439-011-0269-6.
[14] Kastyak-Ibrahim MZ, Di Curzio DL, Buist R, Herrera SL, Albensi BC, Del Bigio MR, et al. Neurofibrillary tangles and plaques are not accompanied by white matter pathology in aged triple transgenic-Alzheimer disease mice. Magn Reson Imaging 2013;31:1515–21. https://doi.org/10.1016/j.mri.2013.06.013.
[15] Snow WM, Dale R, O'Brien-Moran Z, Buist R, Peirson D, Martin M, et al. In vivo detection of gray matter neuropathology in the 3xTg mouse model of Alzheimer's disease with diffusion tensor imaging. J Alzheimers Dis 2017;58:841–53. https://doi.org/10.3233/JAD-170136.
[16] Oddo S, Caccamo A, Kitazawa M, Tseng BP, Laferla FM. Amyloid deposition precedes tangle formation in a triple transgenic model of Alzheimer's disease. Neurobiol Aging 2003;24:1063–70.
[17] Desai MK, Sudol KL, Janelsins MC, Mastrangelo MA, Frazer ME, Bowers WJ. Triple-transgenic Alzheimer's disease mice exhibit region-specific abnormalities in brain myelination patterns prior to appearance of amyloid and tau pathology. Glia 2009;57:54–65. https://doi.org/10.1002/glia.20734.
[18] Desai MK, Mastrangelo MA, Ryan DA, Sudol KL, Narrow WC, Bowers WJ. Early oligodendrocyte/myelin pathology in Alzheimer's disease mice constitutes a novel therapeutic target. Am J Pathol 2010;177:1422–35. https://doi.org/10.2353/ajpath.2010.100087.
[19] Desai MK, Guercio BJ, Narrow WC, Bowers WJ. An Alzheimer's disease-relevant presenilin-1 mutation augments amyloid-beta-induced oligodendrocyte dysfunction. Glia 2011;59:627–40. https://doi.org/10.1002/glia.21131.
[20] Jensen JH, Helpern JA, Ramani A, Lu H, Kaczynski K. Diffusional kurtosis imaging: the quantification of non-Gaussian water diffusion by means of magnetic resonance imaging. Magn Reson Med 2005;53:1432–40. https://doi.org/10.1002/mrm.20508.
[21] Jensen JH, Helpern JA. MRI quantification of non-Gaussian water diffusion by kurtosis analysis. NMR Biomed 2010;23:698–710. https://doi.org/10.1002/nbm.1518.
[22] Falangola MF, Jensen JH, Babb JS, Hu C, Castellanos FX, Di Martino A, et al. Age-related non-Gaussian diffusion patterns in the prefrontal brain. J Magn Reson Imaging 2008;28:1345–50. https://doi.org/10.1002/jmri.21604.
[23] Gong NJ, Wong CS, Chan CC, Leung LM, Chu YC. Aging in deep gray matter and white matter revealed by diffusional kurtosis imaging. Neurobiol Aging 2014;35:2203–16. https://doi.org/10.1016/j.neurobiolaging.2014.03.011.
[24] Das SK, Wang JL, Bing L, Bhetuwal A, Yang HF. Regional values of diffusional kurtosis estimates in the healthy brain during Normal aging. Clin Neuroradiol 2017;27:283–98. https://doi.org/10.1007/s00062-015-0490-z.
[25] Coutu JP, Chen JJ, Rosas HD, Salat DH. Non-Gaussian water diffusion in aging white matter. Neurobiol Aging 2014;35:1412–21. https://doi.org/10.1016/j.neurobiolaging.2013.12.001.
[26] Struyfs H, Van Hecke W, Veraart J, Sijbers J, Slaets S, De Belder M, et al. Diffusion kurtosis imaging: a possible MRI biomarker for AD diagnosis? J Alzheimers Dis 2015;48:937–48. https://doi.org/10.3233/JAD-150253.
[27] Yuan L, Sun M, Chen Y, Long M, Zhao X, Yin J, et al. Non-Gaussian diffusion alterations on diffusion kurtosis imaging in patients with early Alzheimer's disease. Neurosci Lett 2016;616:11–8. https://doi.org/10.1016/j.neulet.2016.01.021.
[28] Fieremans E, Jensen JH, Helpern JA. White matter characterization with diffusional kurtosis imaging. Neuroimage 2011;58:177–88. https://doi.org/10.1016/j.neuroimage.2011.06.006.
[29] Fieremans E, Benitez A, Jensen JH, Falangola MF, Tabesh A, Deardorff RL, et al. Novel white matter tract integrity metrics sensitive to Alzheimer disease progression. AJNR Am J Neuroradiol 2013;34:2105–12. https://doi.org/10.3174/ajnr.A3553.
[30] Benitez A, Fieremans E, Jensen JH, Falangola MF, Tabesh A, Ferris SH, et al. White matter tract integrity metrics reflect the vulnerability of late-myelinating tracts in Alzheimer's disease. Neuroimage Clin 2014;4:64–71. https://doi.org/10.1016/j.nicl.2013.11.001.
[31] Benitez A, Jensen JH, Falangola MF, Nietert PJ, Helpern JA. Modeling white matter tract integrity in aging with diffusional kurtosis imaging. Neurobiol Aging 2018;70:265–75.
[32] Cheung MM, Hui ES, Chan KC, Helpern JA, Qi L, Wu EX. Does diffusion kurtosis imaging lead to better neural tissue characterization? A rodent brain maturation study. Neuroimage 2009;45:386–92. https://doi.org/10.1016/j.neuroimage.2008.12.018.
[33] Falangola MF, Guilfoyle DN, Tabesh A, Hui ES, Nie X, Jensen JH, et al. Histological correlation of diffusional kurtosis and white matter modeling metrics in cuprizone-induced corpus callosum demyelination. NMR Biomed 2014;27:948–57. https://doi.org/10.1002/nbm.3140.
[34] Nie X, Hamlett ED, Granholm AC, Hui ES, Helpern JA, Jensen JH, et al. Evidence of altered age-related brain cytoarchitecture in mouse models of down syndrome: a diffusional kurtosis imaging study. Magn Reson Imaging 2015;33:437–47. https://doi.org/10.1016/j.mri.2014.12.008.

[35] Vanhoutte G, Pereson S, Delgado YPR, Guns PJ, Asselbergh B, Veraart J, et al. Diffusion kurtosis imaging to detect amyloidosis in an APP/PS1 mouse model for Alzheimer's disease. Magn Reson Med 2013;69:1115–21. https://doi.org/10.1002/mrm.24680.
[36] Praet J, Manyakov NV, Muchene L, Mai Z, Terzopoulos V, de Backer S, et al. Diffusion kurtosis imaging allows the early detection and longitudinal follow-up of amyloid-beta-induced pathology. Alzheimers Res Ther 2018;10(1). https://doi.org/10.1186/s13195-017-0329-8.
[37] Tabesh A, Jensen JH, Ardekani BA, Helpern JA. Estimation of tensors and tensor-derived measures in diffusional kurtosis imaging. Magn Reson Med 2011;65:823–36. https://doi.org/10.1002/mrm.22655.
[38] Lu H, Jensen JH, Ramani A, Helpern JA. Three-dimensional characterization of non-Gaussian water diffusion in humans using diffusion kurtosis imaging. NMR Biomed 2006;19:236–47. https://doi.org/10.1002/nbm.1020.
[39] Glenn GR, Helpern JA, Tabesh A, Jensen JH. Quantitative assessment of diffusional kurtosis anisotropy. NMR Biomed 2015;28:448–59. https://doi.org/10.1002/nbm.3271.
[40] Veraart J, Poot DH, Van Hecke W, Blockx I, Van der Linden A, Verhoye M, et al. More accurate estimation of diffusion tensor parameters using diffusion kurtosis imaging. Magn Reson Med 2011;65:138–45. https://doi.org/10.1002/mrm.22603.
[41] Schneider CA, Rasband WS, Eliceiri KW. NIH image to ImageJ: 25 years of image analysis. Nat Methods 2012 Jun 28;9(7):671.
[42] Paxinos G, Franklin KBJ. The mouse brain in stereotaxic coordinates. Compact 2n. Amsterdam; Boston: Elsevier Academic Press; 2004.
[43] Akaike H. A new look at the statistical model identification. IEEE Trans Autom Control 1974;19:716–23. https://doi.org/10.1109/TAC.1974.1100705.
[44] Yoshida S, Oishi K, Faria AV, Mori S. Diffusion tensor imaging of normal brain development. Pediatr Radiol 2013;43:15–27. https://doi.org/10.1007/s00247-012-2496-x.
[45] Sun SW, Song SK, Harms MP, Lin SJ, Holtzman DM, Merchant KM, et al. Detection of age-dependent brain injury in a mouse model of brain amyloidosis associated with Alzheimer's disease using magnetic resonance diffusion tensor imaging. Exp Neurol 2005;191:77–85. https://doi.org/10.1016/j.expneurol.2004.09.006.
[46] Sahara N, Perez PD, Lin WL, Dickson DW, Ren Y, Zeng H, et al. Age-related decline in white matter integrity in a mouse model of tauopathy: an in vivo diffusion tensor magnetic resonance imaging study. Neurobiol Aging 2014;35:1364–74. https://doi.org/10.1016/j.neurobiolaging.2013.12.009.
[47] Hirata-Fukae C, Li HF, Hoe HS, Gray AJ, Minami SS, Hamada K, et al. Females exhibit more extensive amyloid, but not tau, pathology in an Alzheimer transgenic model. Brain Res 2008;1216:92–103. https://doi.org/10.1016/j.brainres.2008.03.079.
[48] Carroll JC, Rosario ER, Kreimer S, Villamagna A, Gentzschein E, Stanczyk FZ, et al. Sex differences in β-amyloid accumulation in 3xTg-AD mice: role of neonatal sex steroid hormone exposure. Brain Res 2010 Dec 17;1366:233–45. https://doi.org/10.1016/j.brainres.2010.10.009.
[49] Thomas AG, Koumellis P, Dineen RA. The fornix in health and disease: an imaging review. Radiographics 2011;31:1107–21. https://doi.org/10.1148/rg.314105729.
[50] Amaral RSC, Park MTM, Devenyi GA, Lynn V, Pipitone J, Winterburn J, et al. Manual segmentation of the fornix, fimbria, and alveus on high-resolution 3 T MRI: application via fully-automated mapping of the human memory circuit white and grey matter in healthy and pathological aging. Neuroimage 2018;170:132–50. https://doi.org/10.1016/j.neuroimage.2016.10.027.
[51] Gonzalez-Lima F, Berndt JD, Valla JE, Games D, Reiman EM. Reduced corpus callosum, fornix and hippocampus in PDAPP transgenic mouse model of Alzheimer's disease. Neuroreport 2001;12:2375–9.
[52] Jang SH, Cho SH, Chang MC. Age-related degeneration of the fornix in the human brain: a diffusion tensor imaging study. Int J Neurosci 2011;121:94–100. https://doi.org/10.3109/00207454.2010.531894.
[53] Amlien IK, Fjell AM. Diffusion tensor imaging of white matter degeneration in Alzheimer's disease and mild cognitive impairment. Neuroscience 2014;276:206–15. https://doi.org/10.1016/j.neuroscience.2014.02.017.
[54] Chen DQ, Strauss I, Hayes DJ, Davis KD, Hodaie M. Age-related changes in diffusion tensor imaging metrics of fornix subregions in healthy humans. Stereotact Funct Neurosurg 2015;93:151–9. https://doi.org/10.1159/000368442.
[55] Badea A, Kane L, Anderson RJ, Qi Y, Foster M, Cofer GP, et al. The fornix provides multiple biomarkers to characterize circuit disruption in a mouse model of Alzheimer's disease. Neuroimage 2016;142:498–511. https://doi.org/10.1016/j.neuroimage.2016.08.014.